

Observations and simulations of the ionospheric and thermospheric response to the December 2006 geomagnetic storm: Initial phase

Jiuhou Lei,¹ Wenbin Wang,¹ Alan G. Burns,¹ Stanley C. Solomon,¹ Arthur D. Richmond,¹ Mike Wiltberger,¹ Larisa P. Goncharenko,² Anthea Coster,² and Bodo W. Reinisch³

Received 10 September 2007; revised 3 October 2007; accepted 18 October 2007; published 25 January 2008.

[1] We have investigated the thermospheric and ionospheric response to the 14–15 December 2006 geomagnetic storm using a Coupled Magnetosphere Ionosphere Thermosphere (CMIT) 2.0 model simulation. In this paper we focus on observations and simulations during the initial phase of the storm (about 8 h), when the shock was driving changes in geospace. The global ionospheric maps of total electron content (TEC), ionosonde data at four stations and Millstone Hill incoherent scatter radar (ISR) observations are compared with the corresponding simulation results from the CMIT model. The observations showed significant positive storm effects occurred in the Atlantic sector after the onset of this storm. The CMIT model is able to capture the temporal and spatial variations of the ionospheric storm effects seen in the GPS TEC observations, although the model slightly underestimates the daytime positive ionospheric storm in the South American sector. The simulations are also in agreement with the ionosonde and ISR ionospheric measurements. Term analysis of the ion continuity equation demonstrates that changes in the electric fields play a dominant role in generating the observed ionospheric positive storm effect in the American sector during the initial phase, although neutral winds and composition changes also contribute. The difference in the strength of the enhancements over North and South America can be explained by the slope of the topside electron density profiles in the two hemispheres. In the southern hemisphere electron densities decrease slowly with altitude, whereas the decrease is much more rapid in the northern (winter) hemisphere. The electric fields, therefore, cannot cause large increases in electron density by uplifting the plasma, so positive storm effects are small in the southern hemisphere compared with the northern hemisphere, even though the increase in $h_m F_2$ is greater in the southern hemisphere. Nighttime changes in electron density in other longitude sectors are small, because the topside electron densities also decrease slowly with altitude at night.

Citation: Lei, J., W. Wang, A. G. Burns, S. C. Solomon, A. D. Richmond, M. Wiltberger, L. P. Goncharenko, A. Coster, and B. W. Reinisch (2008), Observations and simulations of the ionospheric and thermospheric response to the December 2006 geomagnetic storm: Initial phase, *J. Geophys. Res.*, 113, A01314, doi:10.1029/2007JA012807.

1. Introduction

[2] Ionospheric storms are an extreme form of ‘space weather’ resulting from magnetosphere-ionosphere-thermosphere coupling, and are considered as the most complicated phenomenon in the ionosphere-thermosphere (I-T) system [Buonsanto, 1999; Szuszczewicz et al., 1998]. During geomagnetic storms, the significantly enhanced injection of energy from the solar wind and magnetosphere leads to large changes in the chemistry and dynamics of the high

latitude I-T system [e.g., Prölss, 1995; Lu et al., 1995; Buonsanto, 1999], which then significantly influences the global I-T system through various dynamic/electrodynamical processes. As a result, large disturbances in ionospheric electron densities and total electron content (TEC) take place during geomagnetic storms [e.g., Prölss, 1995; Buonsanto, 1999; Mendillo, 2006]. Storm-time ionospheric electron densities or TEC can either decrease (negative effects) or increase (positive effects), compared to the quiet time ionosphere.

[3] Many efforts have been made to study the ionospheric response to geomagnetic storms using both observations and theoretical models [see the references in the recent review papers, Prölss, 1995; Buonsanto, 1999; Danilov and Lastovička, 2001; Mendillo, 2006; Burns et al., 2007]. The mechanisms that drive these ionospheric storm effects, which can be changes in neutral composition, neutral winds, electric fields and other horizontal transport, are very

¹High Altitude Observatory, National Center for Atmospheric Research, Boulder, Colorado, USA.

²Haystack Observatory, Massachusetts Institute of Technology, Westford, Massachusetts, USA.

³Center for Atmospheric Research, University of Massachusetts, Lowell, Massachusetts, USA.

complicated [Prölss, 1995; Buonsanto, 1999]. Usually, some of these mechanisms work together to produce the observed storm effects, and their relative importance differs from case to case. Furthermore, the mechanisms of ionospheric storm effects can vary significantly with location (latitude) and the phase of storm [Prölss, 1995].

[4] Prölss [1993a, 1993b] proposed that the observed daytime positive storm effects, especially during the initial phase, are caused by traveling atmospheric disturbances (TADs) and suggested that the electrodynamic mechanism proposed by earlier work was not as important a mechanism as thermospheric dynamics [Prölss, 1995]. However, Prölss [1995] asked in his review paper, “are external electric fields of secondary importance when it comes to explaining short-duration positive storm effects at middle latitudes?” and “is the assumption correct that TADs are a more likely explanation for sudden height rises in the day- and nightside ionospheres?” Furthermore, he also raised the question that “is it correct to assume that neutral composition changes play a secondary role when it comes to explaining positive storm effects at middle latitudes?” Thus the importance of electric fields and neutral composition for the positive ionospheric storm phase is not fully understood, and the explanation of positive storm effects is still a great challenge in ionospheric science [Burns *et al.*, 2007]. This paper will attempt to address parts of these issues.

[5] We will focus on ionospheric positive storm effects during the initial phase of the December 2006 geomagnetic storm. The Coupled Magnetosphere-Ionosphere-Thermosphere Model (CMIT) is used to investigate the ionospheric and thermospheric response to this geomagnetic storm. Note that the CMIT model can self-consistently simulate the effects of neutral composition, neutral winds, dynamo and penetration electric fields on the ionosphere. This coupled model is used in this paper to examine the importance of these processes to ionospheric storm effects during the initial phase of the 14th and 15th December 2006 geomagnetic storm.

[6] The rest of the paper is organized as follows. The Coupled Magnetosphere-Ionosphere-Thermosphere Model (CMIT) is described in section 2, followed by a description of solar geophysical conditions of the December 2006 storm in section 3. The observations and model simulations of ionospheric storm effects and their comparisons during the initial phase are presented in section 4, and the analysis of the processes causing ionospheric storm effects is given in section 5. Conclusions are drawn in section 6.

2. Coupled Magnetosphere-Ionosphere-Thermosphere Model (CMIT)

[7] The latest version of Coupled Magnetosphere-Ionosphere-Thermosphere Model (CMIT 2.0) is used in this study. The CMIT 2.0 model combines the National Center for Atmospheric Research Thermosphere-Ionosphere-Electrodynamics General Circulation Model (NCAR-TIEGCM) with the Lyon-Fedder-Mobarry (LFM) global magnetohydrodynamic (MHD) magnetospheric model [Wiltberger *et al.*, 2004; Wang *et al.*, 2004]. The NCAR-TIEGCM [Roble *et al.*, 1988; Richmond *et al.*, 1992] is a time dependent, three-dimensional model that solves the fully coupled, nonlinear, hydrodynamic, thermodynamic, and continuity

equations of the neutral gas self-consistently with the ion energy, ion momentum, and ion continuity equations using a finite differencing scheme for spatial and temporal variations. It has 29 constant-pressure levels in the vertical extending from approximately 97 km to 500–700 km in altitude. The input parameters for the NCAR-TIEGCM model are solar EUV and UV spectral fluxes, parameterized by the $F_{10.7}$ index, auroral particle precipitation, an imposed magnetospheric electric field, and the amplitudes and phases of tides from the lower atmosphere.

[8] The LFM code solves the ideal MHD equations for the magnetosphere in a conservative form using the Partial Interface Method on a distorted spherical mesh and Yee type grid [Lyon *et al.*, 2004]. Its domain extends from 30 R_E upstream to $-300 R_E$ tailward of the Earth in the X direction (R_E is the radius of the Earth). Its other boundaries (Y and Z directions) extend to $\pm 100 R_E$ from the Earth in both the Y and Z planes. There is an additional boundary around the Earth that is typically specified at 3 R_E , but can be lowered to 2 R_E . Different conditions are applied to the various boundaries. Solar wind data are used for the upstream and side (Y and Z) boundaries. Supersonic outflow is assumed at the downstream (away from the Sun on the Sun-Earth axis) boundary. The default specification at the inner boundary is to use an empirical description of ionospheric conductivities [Fedder *et al.*, 1995] assuming that the ionosphere can be represented as a thin spherical shell.

[9] In the CMIT model, LFM provides auroral particle precipitation and magnetospheric electric fields to the TIEGCM; whereas, the LFM model uses the height integrated Pedersen and Hall conductivities from the TIEGCM, instead of using empirical ionospheric conductivities [Wiltberger *et al.*, 2004; Wang *et al.*, 2004]. The coupling between the LFM and the TIEGCM has been undertaken in many steps. Wiltberger *et al.* [2004] and Wang *et al.* [2004] reported the magnetospheric, thermospheric and ionospheric responses under idealized solar winds condition using the CMIT 1.0 model, which successfully coupled the LFM model with the thermosphere-ionosphere nested grid (TING) model. Recently, Wang *et al.* [2006] have included the effects of thermospheric neutral winds on the magnetosphere. The latest step is the coupling of the NCAR-TIEGCM with the LFM model. The CMIT 2.0 model has been able to capture the temporal variations of the vertical ion drifts seen in Jicamarca radar measurements [Wang *et al.*, unpublished manuscript, 2007].

3. Solar Wind and Geophysical Conditions

[10] Figure 1 shows solar wind speed, interplanetary magnetic field B_z , AE index, and A_p and D_{st} index during 13–15 December 2006. The interplanetary magnetic field (IMF) parameters (in GSM coordinates) were measured by the WIND satellite, which was located 248 \sim 252 R_E upstream of the Earth during this period. The solar wind data were shifted by 30 minutes to account for the time that it took for the solar wind to propagate from the satellite location to the magnetopause. Note that observations from the ACE satellite were not used in this study because of a data gap in the ACE data due to the effects of the storm. This does not present a problem as the measurements from

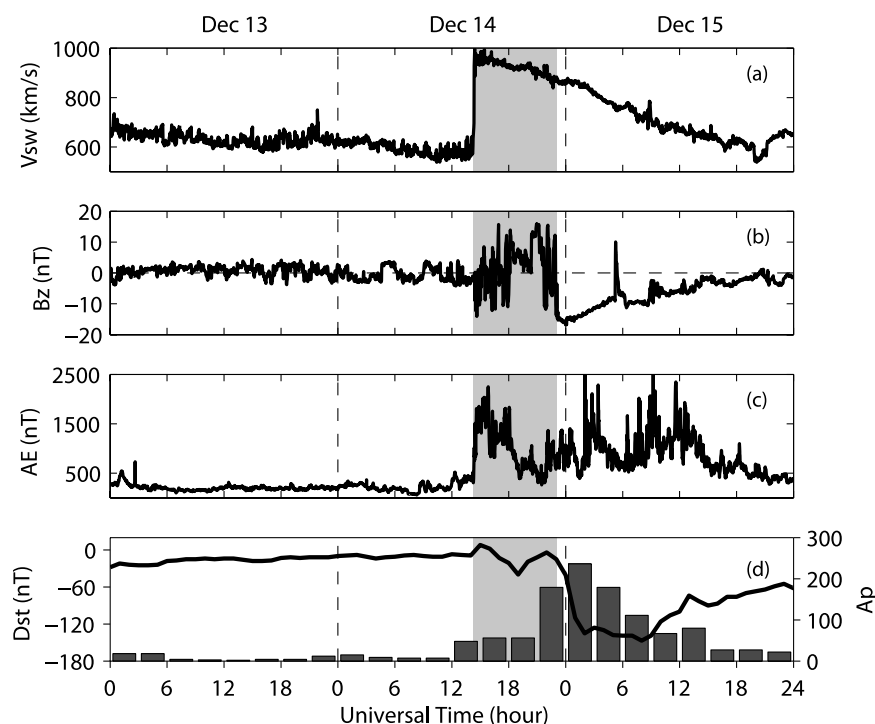


Figure 1. (a) Solar wind speed, (b) interplanetary magnetic field B_z , (c) AE index, (d) A_p and D_{st} index on 13–15 December 2006. The patches indicate the initial phase of this storm.

the two satellites for the rest of this event were in good agreement.

[11] A shock occurred at 1340 UT (unshifted time) on 14 December at the WIND satellite location (the time referred hereafter is the shifted time), which was indicated by an abrupt solar wind speed increase from 650 km/s to 980 km/s. After the initial shock, the solar wind speed underwent a gradual decrease. The B_z component started to oscillate after the arrival of the shock, and continued to do so for a few hours. After 1800 UT on 14 December, B_z became northward and it continued to undergo fast oscillations before its rapid southward turning at 2300 UT on 14 December, which corresponded to the beginning of the main phase of this storm.

[12] The AE index shows that auroral electrojet activity became strong after the arrival of the shock, and continued to be strong until about 1500 UT on 15 December, indicating intense activity on 14–15 December. The sudden storm commencement (SSC) for this storm occurred at \sim 1414 UT on 14 December (<http://www.ngdc.noaa.gov/stp/SOLAR/ftpSSC.html>). D_{st} went down to -147 nT at 0800 UT on 15 December, and then started to recover. The D_{st} minimum value of -147 nT shows that this storm was intense [Gonzalez *et al.*, 1994]. A_p values increased after the SSC to a maximum of 236 at 0000–0300 UT on 15 December. Note that A_p and AE values were relatively low on 13 December, so we will use the ionospheric parameters on 13 December as the quiet time reference.

[13] A storm can usually be divided into the initial, main and recovery phases. In this paper, we will focus on the ionospheric storm effects during the initial phase of the December 2006 storm where geomagnetic activity is mainly controlled by the shock, before the main phase of the storm.

Note that the initial phase of this storm between 1414 and 2300 UT on 14 December is marked by the shaded patches in Figure 1.

4. Observations and Simulations

[14] In this section, we will compare the ground-based GPS TEC data and the ionosonde and Millstone Hill incoherent scatter radar (ISR) observations with simulation results from the CMIT model. The GPS TEC data used here were provided by the Madrigal database at MIT Haystack Observatory (<http://www.openmadrigal.org>). The detailed descriptions about the technique of processing GPS data can be found in *Rideout and Coster* [2006]. The Digisonde ionogram data, provided by the University of Massachusetts at Lowell, have been manually scaled using UMLCAR SAO-Explorer (<http://ulcar.uml.edu>) to get the F_2 ionospheric characteristics [Reinisch *et al.*, 2005]. The ionosonde data at four stations in the American sector are used in this comparison.

[15] Figure 2 shows global maps of TEC differences with respect to the quiet time background from 1600 to 2200 UT (with an interval of 2 h) on 14 December. The differential TEC maps from GPS observations are compared with those from CMIT simulations. This figure is plotted as a function of geographic latitude and local time; thus the world map shifts with universal time (UT). Positive storm effects can be seen in the data (left panels) over Eastern North America at 1600 UT (about 2 h after the arrival of the shock). Stronger positive storm effects occurred at middle-low latitudes in both the North and South American sectors and the west coast of Africa at 1800 UT. They became more pronounced two hours later, and could be observed over

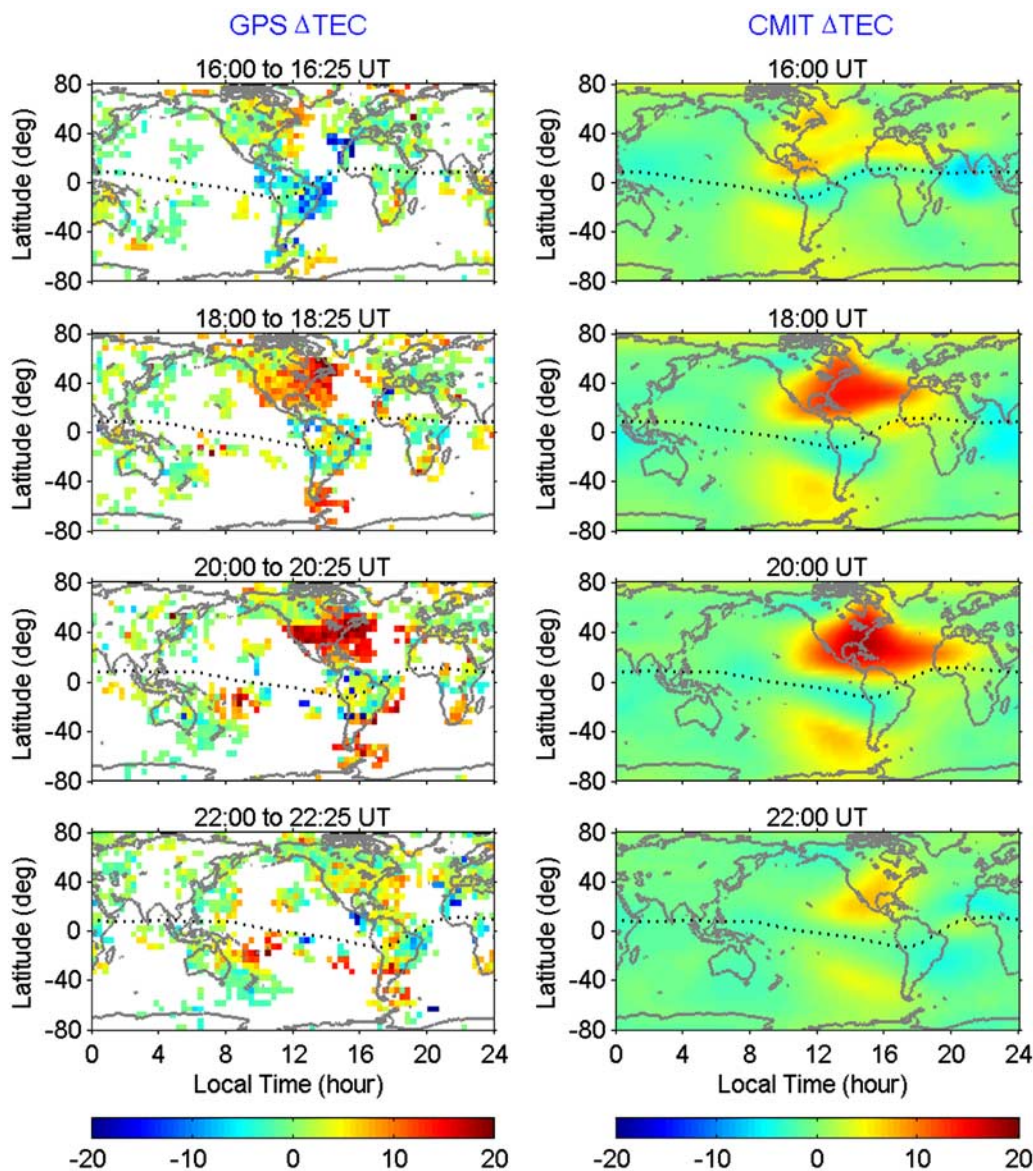


Figure 2. Global maps of differential TEC between the disturbance day (14 December) and quiet day (13 December) from 1600 to 2200 UT. Left panels: GPS observations; right panels: CMIT 2.0 simulation. The unit of differential TEC is TECu ($1 \text{ TECu} = 10^{16} \text{ electrons/m}^2$). The dotted lines indicate the location of the magnetic equator.

large areas at 2000 UT. After that positive storm effects became weaker. Note that the simultaneous enhancement of TEC in the two hemispheres has been reported by *Foster and Coster* [2007].

[16] Weak negative storm effects occurred in the equatorial region of the American and African sectors (near the magnetic equator in particular) during this period. The corresponding simulation results from the CMIT model are shown in the right panels of Figure 2. The model captured the temporal and spatial variations of the ionospheric storm effects seen in the GPS TEC observations (left panels of Figure 2). Good agreement was also obtained for the magnitude of TEC changes. Interestingly, this coupled model produced a tongue of ionization at middle-high latitudes in North America from 1600 to 2000 UT. This feature seems to appear in the observations, but unfortu-

nately the TEC observations in the Atlantic Ocean region were sparse. Note that there are also some differences between the GPS TEC observations and model simulations. Specifically, the CMIT model underestimates positive storm effects in the South American sector.

[17] Besides TEC, the peak density (N_mF_2) and peak height (h_mF_2) at the F_2 region are often used to examine ionospheric storm effects. Figure 3 shows global maps of differential N_mF_2 and h_mF_2 from the CMIT simulations between 14 and 13 December from 1600 to 2200 UT. As expected, the temporal and spatial variations of the ionospheric storm effects in N_mF_2 are very similar with those in TEC (right panels, Figure 2) because the simulated TEC values are primarily produced from the densities at the F_2 peak up to one scale height above this peak. However, the negative storm effects in N_mF_2 are a little stronger than

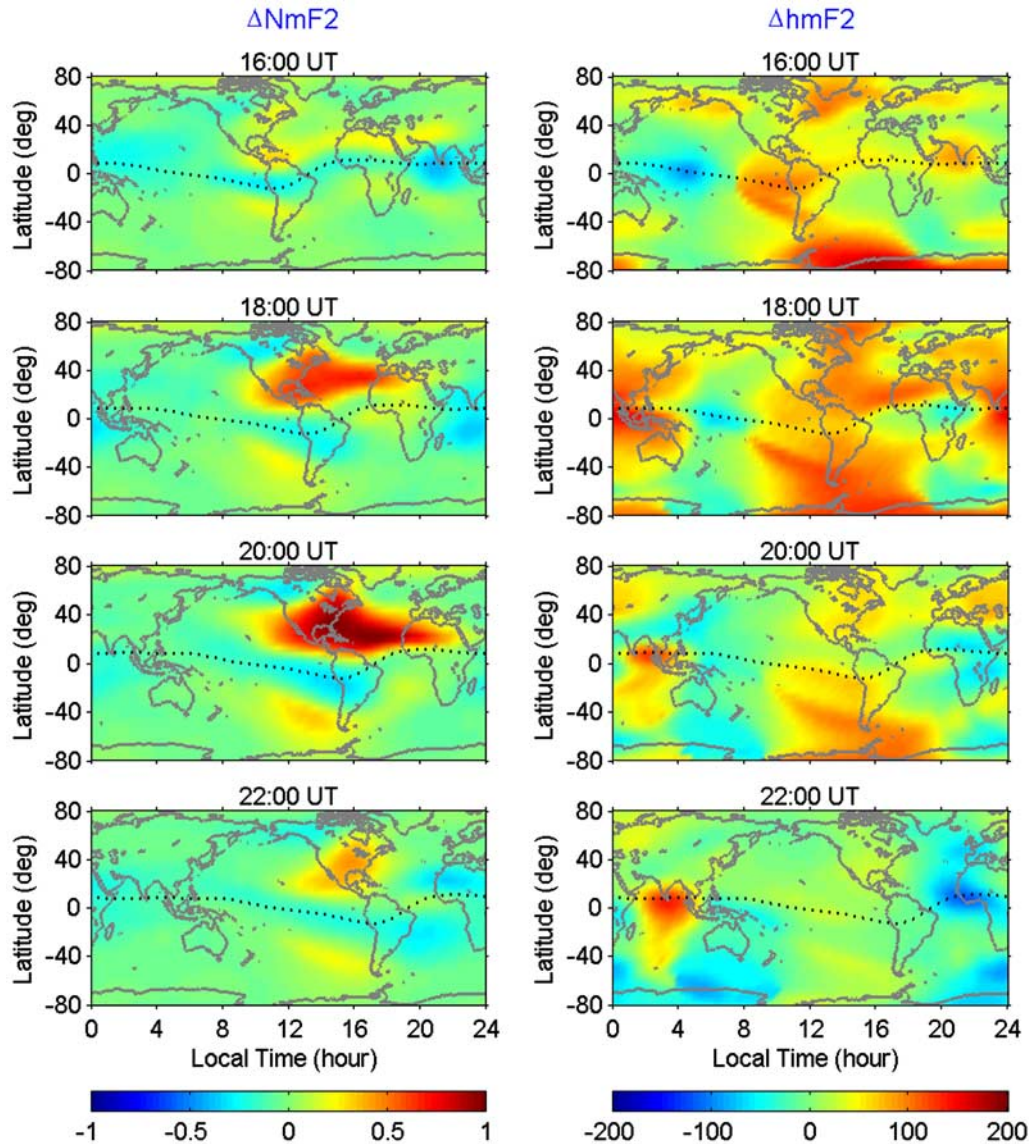


Figure 3. Global maps of differential peak density (left, in units of 10^{12} m^{-3}) and peak height (right, in units of km) from the CMIT simulations between the disturbance day (14 December) and quiet day (13 December). The dotted lines indicate the location of the magnetic equator.

those shown in TEC. $h_m F_2$, as illustrated in the right side of Figure 3, increases in both the daytime and nighttime sectors from 1600 to 2000 UT; it then begins to recover at 2200 UT. $h_m F_2$ increases significantly in both hemispheres in the American sector. The increment of $h_m F_2$ by about 200 km at middle and high latitudes in the Southern Hemisphere is much greater than that in the Northern Hemisphere from 1600 to 2000 UT. However, it is surprising that the increase of $N_m F_2$ (or TEC) is much smaller in the Southern Hemisphere than in the Northern Hemisphere. The hemispheric asymmetry of the simulated positive storm effects in the American sector will be further discussed in section 5. $h_m F_2$ also increases in a large area at night; however, nighttime electron densities do not show obvious changes.

[18] From Figures 2–3, it is interesting to see that the very strong positive storm effects over North America at

2000 UT almost disappeared in just 2–3 h. The recovery time of the positive storm effects during this initial phase is consistent with the e -folding time reported by *Jee et al.* [2007]. They used the electron densities from the Global Assimilation of Ionospheric Measurements (GAIM) model to initialize the ionospheric part of the Thermosphere Ionosphere Nested Grid (TING) model, and found the e -folding time of the initialization is about $2 \sim 3$ h for most conditions if the thermosphere was not disturbed. This suggests that the thermosphere during the initial phase was not disturbed severely to produce a typical post main phase recovery period that can usually last one or more days [Prolss, 1995; Mendillo, 2006; Burns et al., 2007].

[19] Figure 4 shows the variations of $N_m F_2$ and $h_m F_2$ on 13–14 December from both ionosonde measurements and CMIT simulations at four stations in the North American sector. These stations are: Wallops Island (37.9°N , 75.5°W),

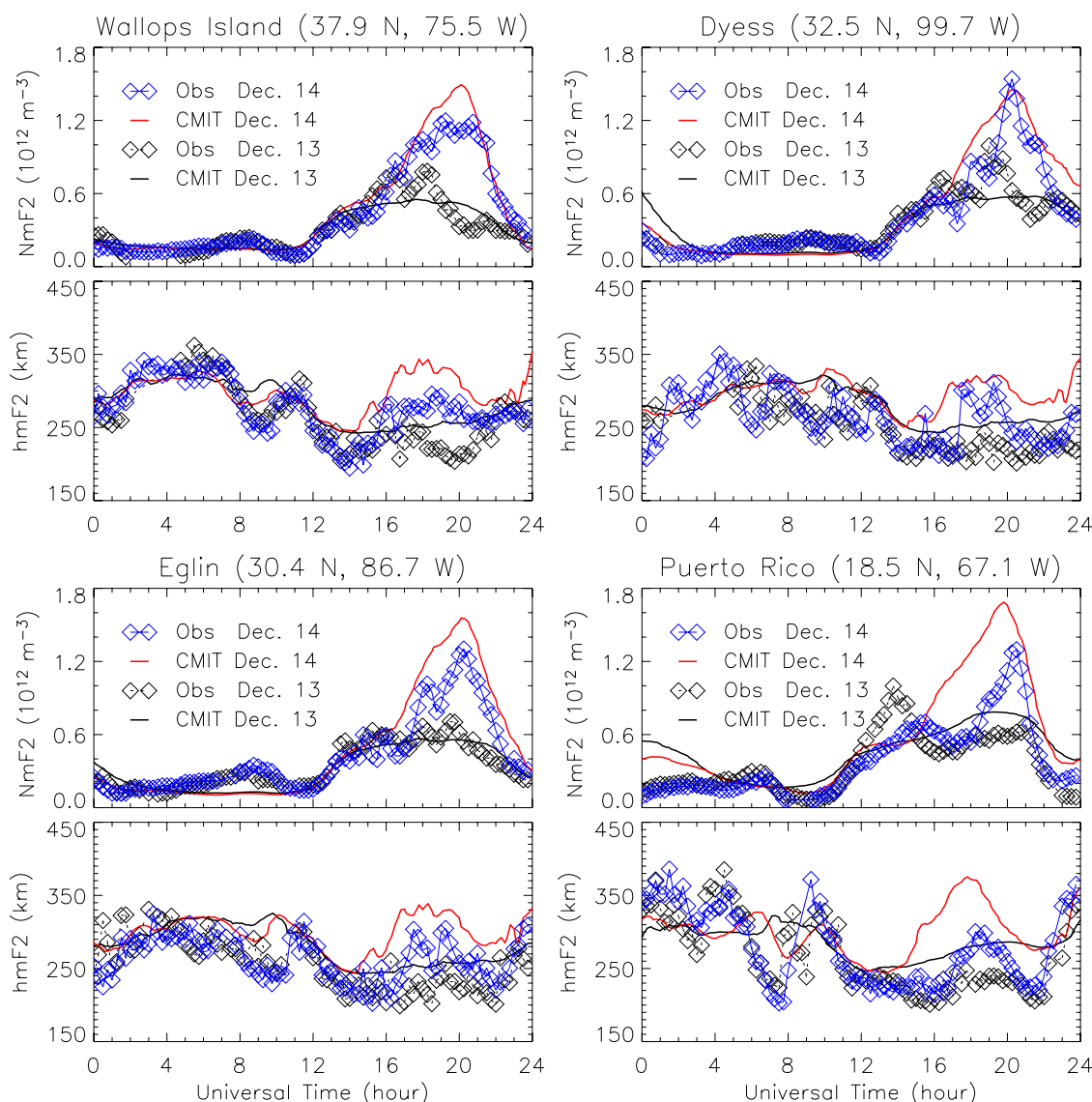


Figure 4. Comparison of the peak density N_mF_2 and peak height h_mF_2 obtained from the ionosonde measurements (at Wallops Island, Dyess, Eglin and Puerto Rico) with the corresponding CMIT simulations. The dash with diamonds and solid lines with diamonds stand for the observations on 13 and 14 December; and the black and red solid lines for the CMIT simulations on 13 and 14 December, respectively.

Dyess (32.5°N, 99.7°W), Eglin (30.4°N, 86.7°W) and Puerto Rico (18.5°N, 67.1°W). First we concentrate on the storm effects in the ionosonde data. N_mF_2 and h_mF_2 values were greater after the onset of the storm on 14 December than they were on the quiet day. For example, at Wallops Island, N_mF_2 increased from 1600 to 2300 UT. Therefore the increases in the F_2 region electron density at this station lasted for about 7 h, and can be termed a long-duration positive storm phase [Bauske and Pröls, 1998]. At 1900 UT N_mF_2 was greater by a factor of about 3 than its quiet time value and h_mF_2 was about 90 km higher. These storm features prevailed at the other three stations as well. These variations in electron density are consistent with those of the GPS TEC data (Figure 2).

[20] Now we turn to the simulation results in Figure 4. We can see that the modeled increments of N_mF_2 and h_mF_2

are in agreement with those from the observations, although the model overestimates absolute daytime h_mF_2 at four stations and N_mF_2 values at Puerto Rico from 1700 to 2000 UT. More accurate inputs (including high-latitude coupling and tides/waves) and higher model resolution are probably needed to capture the detailed variations (e.g., short period oscillations) that were seen in the observations. However, the model reproduces the major observed ionospheric features of the storm-time response well.

[21] The ISR at Millstone Hill (42.6°N, 71.5°W) was also operating during this storm. Figure 5 shows the F_2 ionospheric characteristics (N_mF_2 and h_mF_2) from the zenith antenna measurements and vertical electric field drifts at an altitude of about 300 km at Millstone Hill. The CMIT simulation results are also shown in this figure for comparison. Note that the ISR vertical drifts represent the projec-

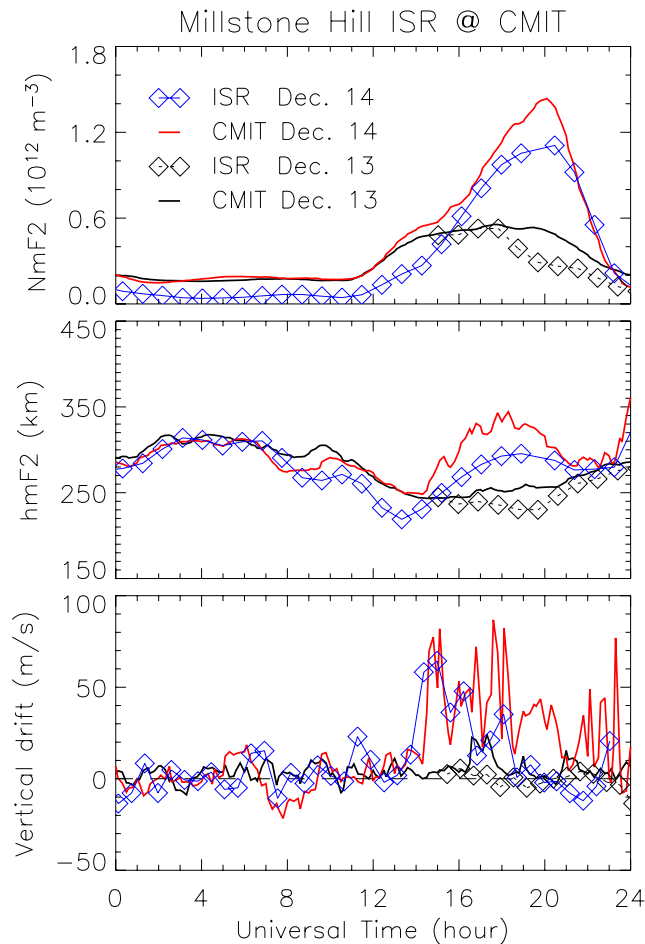


Figure 5. Comparison of N_mF_2 , h_mF_2 and vertical drifts obtained from Millstone Hill incoherent scatter radar measurements with the corresponding CMIT simulations on 13 and 14 December. The legend of this figure is the same as that of Figure 4.

tion of ion drifts in the vertical direction rather than the field-aligned component. The ISR ion drifts were obtained from the line-of-sight velocities between 230 and 400 km, using the zenith antenna and the steerable antenna measurements [Buonsanto and Witasse, 1999]. As shown in Figure 5, there were h_mF_2 and N_mF_2 increases in the afternoon on 14 December, and the increase in N_mF_2 lasted more than 7 h from 1530 to 2300 UT. The variations of h_mF_2 and N_mF_2 at Millstone Hill were similar to those at Wallops Island (Figure 4). Again, there is reasonable agreement between the observed and CMIT model predicted N_mF_2 and h_mF_2 at Millstone Hill. From the bottom panel of Figure 5, it is clear that the ISR vertical ion drifts were greatly enhanced from 1400 UT on 13 December till 1900 UT on 14 December with a maximum velocity of about 60 m/s. Upward ion drifts raise the F region ionization to higher altitudes, where the O^+ loss coefficient becomes relatively low, which should result in higher electron densities. The relative importance of thermospheric winds and composition, with respect to electric fields, for this positive ionospheric storm effect will be discussed in section 5. The observed and modeled vertical drifts compare reasonably well except for the period

between 1900 and 2100 UT, when the modeled vertical drifts were significantly larger than those observed. The discrepancies between the model results and the observed drifts during 1900–2100 UT may be due to that the shielding from the LFM model is weaker than the shielding that actually occurs in the Earth’s inner magnetosphere once the region-2 current system becomes established following the onset of a geomagnetic disturbance. However, this point deserves further investigations.

5. Analysis of the Processes Causing Changes in Electron Density

[22] Given that the CMIT model reproduced most of the observed ionospheric storm effects seen during the initial phase, we can use CMIT to explore the mechanisms that cause these ionospheric storm features in this section.

5.1. Ionospheric and Thermospheric Variations in the American Sector

[23] Figure 6 shows the modeled N_mF_2 and h_mF_2 , neutral temperatures, O/N_2 , meridional winds and vertical drifts at model pressure level 2 (roughly at the altitude of 300 km) as a function of geographic latitude and universal time on 13 and 14 December. We choose one particular geographic longitude 75°W , where positive ionospheric storm effects were prominent during the initial phase (see Figure 2). Compared with quiet time values on 13 December, we can see that the neutral gas temperature and composition (O/N_2), horizontal meridional winds (northward, positive) and vertical drifts all vary greatly from 1400 to 2300 UT on 14 December, when electron densities also show significant changes.

[24] First we concentrate on the results in the Northern Hemisphere in Figure 6. Both electron densities and the peak height, h_mF_2 , increase in the Northern Hemisphere during the initial phase. Compared with the quiet time background conditions, neutral temperatures increase by about 50–100 K and the O/N_2 ratio also shows an enhancement from 1500 to 2300 UT on 14 December. During this period, meridional winds (positive northward) become more poleward at high latitudes and less poleward at low-middle latitudes. The vertical drifts exhibit significant increases during the initial phase, especially from 1500 to 1900 UT. As shown in Figure 5, the drifts generally agree with the Millstone Hill ISR observations. The latitudinal attenuation of the vertical $E \times B$ drift from high to low latitudes (Figure 6f) indicates that the electric field is mainly a penetration electric field from high latitudes during this initial storm phase, although it is beyond the scope of this paper to separate the effects of penetration and dynamo electric fields. We know that weaker poleward winds or stronger upward ion drifts during storm time than those during quiet time can result in increases of daytime electron densities at low and middle latitudes. As discussed later, the increased O/N_2 contributes to the positive storm at higher latitudes of the northern hemisphere. Therefore the positive storm during this initial phase is caused by the combined effects of electric fields, neutral winds and also composition changes.

[25] In the Southern Hemisphere (Figure 6), the daytime peak height h_mF_2 increases by about 100 km during the

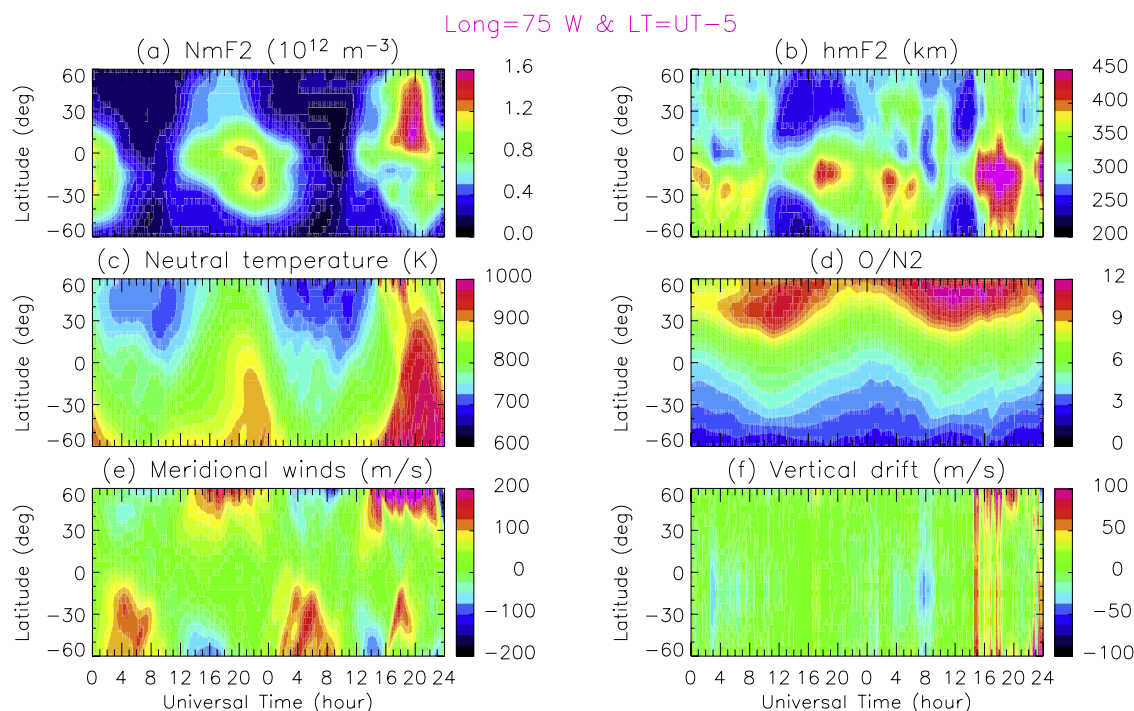


Figure 6. The modeled (a) N_mF_2 and (b) h_mF_2 , (c) neutral temperature, (d) O/N_2 , (e) meridional winds (northward positive), and (f) $E \times B$ vertical drifts (upward positive) at pressure level 2 (about 300 km) as functions of geographic latitude and universal time. The first 24 h are for the quiet day (13 December) and the second for the storm day (14 December). Note the simulation results are presented for the American longitude 75°W (LT = UT-5).

initial phase, but electron densities do not show obvious increases and they even decrease in the southern equatorial anomaly region (Figure 6a). The meridional winds vary from their southward quiet time values (or very weak northward) to strong northward winds during 1600–2100 UT on 14 December. $E \times B$ vertical drifts behave similarly to those in the Northern Hemisphere. The increased northward winds and enhanced vertical drifts can produce the increase of h_mF_2 during storm-time. However, there is little or no increase of daytime electron densities during the initial phase in the Southern Hemisphere. This will be discussed further in section 5.3.

5.2. Global Ionospheric and Thermospheric Changes During the Initial Phase

[26] In section 5.1, we presented the numerical results at one longitude in the American sector to examine the thermosphere and ionosphere response to the storm. A set of global maps are shown in Figure 7 for the differences between storm and quiet time meridional winds, vertical drifts, neutral temperature and O/N_2 from the CMIT simulations for 1600 and 1800 UT. These results can be compared with the ionospheric variations shown in Figures 2–3. We already discussed the thermospheric variations in the daytime sector in detail in section 5.1, so we will now discuss them for the rest of the globe (especially in the night sector).

[27] At 1600 UT, strong upward drifts occur during daytime and downward drifts occur during the night between 2300 and 0500 LT. This suggests that the changes in the zonal electric field are mainly caused by the penetration

of high latitude electric field [see *Tsurutani et al.*, 2004, and references therein]. Changes in nighttime electrical conductivities associated with the elevated evening and depressed early morning ionosphere at 1600 UT, seen in Figure 3, will also alter the generation of nighttime electric fields by the ionospheric wind dynamo, which may be responsible for the low latitude early evening upward and early morning downward drifts seen in Figure 7. *Maruyama et al.* [2005] described the complex manner in which direct penetration and wind-dynamo electric fields can interact. At 1600 UT, the effects of increased equatorward winds and downward drifts at high and middle latitudes tend to cancel out, so h_mF_2 does not change at night. It is interesting to note that the pre-reversal enhancement (PRE) at this UT is very strong. This increased PRE raises the ionosphere near the equator, causing a decrease of electron densities near the equator and a weak increase of electron densities in the equatorial anomalies (see Figure 3 at 1600 UT).

[28] At 1800 UT, drifts are weak and upward in the daytime; the moderate low latitude evening downward and early morning upward drifts may be caused by the disturbed dynamo electric fields associated both with disturbance winds [e.g., *Richmond et al.*, 2003] and disturbed conductivities [e.g., *Maruyama et al.*, 2005]. The increased equatorward winds and upward drifts around midnight and in the early morning cause the significant increase of h_mF_2 in the Asian and European sectors at 1800 UT (Figure 3). At this UT, the vertical drifts during 2000–2100 LT have a significant decrease. As mentioned before, this is quite different at 1600 UT. The strong enhancement of vertical drift at low latitudes at 1600 UT while significant decrease

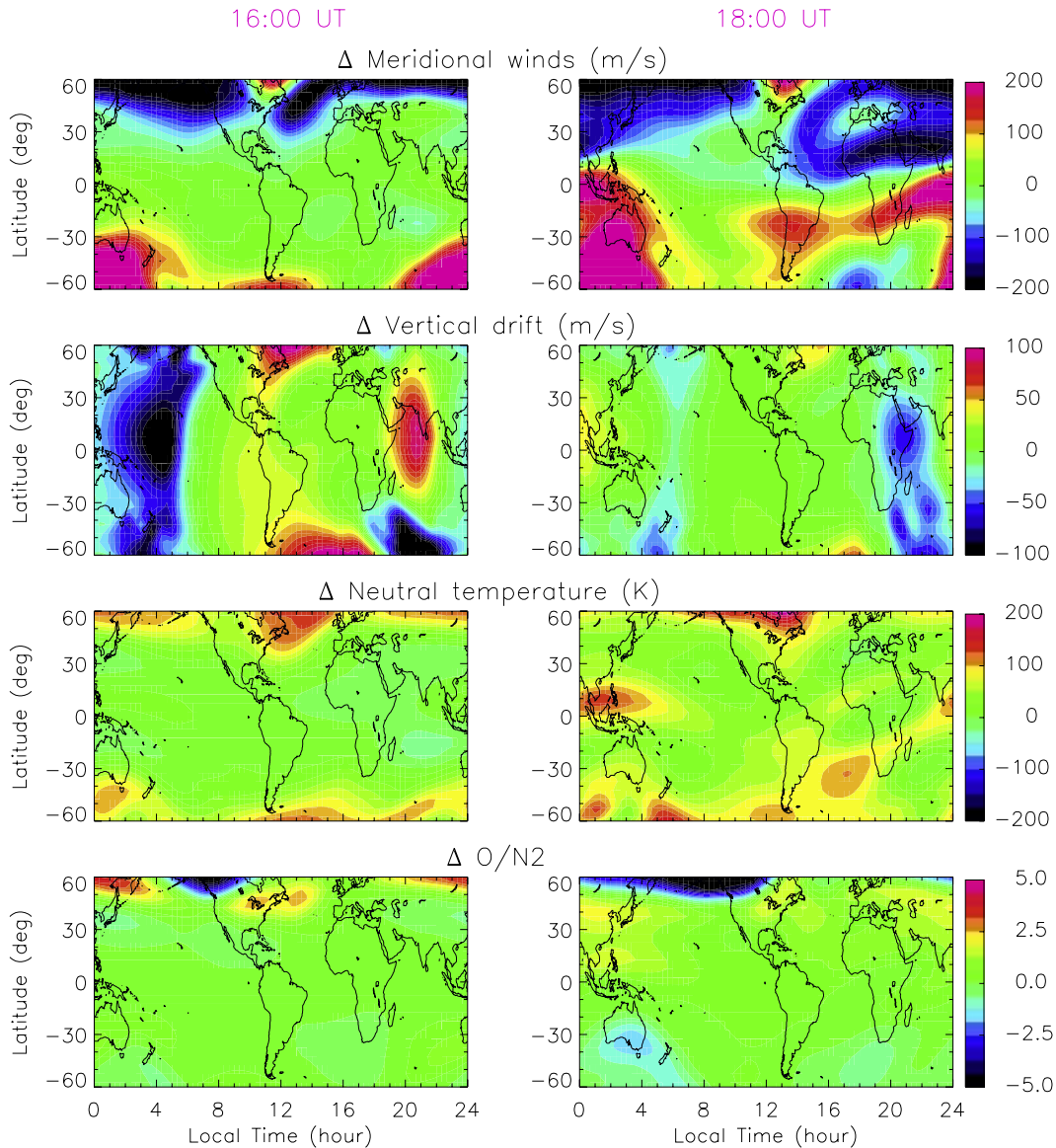


Figure 7. Global maps of differential meridional winds (northward positive), $E \times B$ vertical drifts (upward positive), neutral temperature and O/N_2 at pressure level 2 from the CMIT simulations between the disturbance day (14 December) and quiet day (13 December) for 1600 and 1800 UT (Storm-Quiet).

at 1800 UT may be related to different IMF conditions (see Figure 1). These different IMF conditions may change the global electrodynamics.

[29] Therefore the strongly increased equatorward disturbed thermospheric winds play a major role in producing the increase of $h_m F_2$ at night, whereas electric fields (from both penetration electric fields and disturbed dynamo electric fields) changes also make contributions to the changes of ionospheric peak height during the initial phase.

[30] It is worth noting that the nighttime $N_m F_2$ and TEC do not show obvious increases even though $h_m F_2$ increases significantly at night. This was noted by Prölss [1993b] and was attributed to the absence of solar ionization; Fuller-Rowell *et al.* [1994] explained it by both the absence of solar ionization and low background electron densities at night. However, they did not explain why transport processes are not sufficient to modify electron densities. This issue will be considered further in the next section.

5.3. Term Analysis for the Continuity Equation

[31] As discussed before, both electron densities and $h_m F_2$ change significantly with respect to their quiet time background values after the onset of the storm. The simulation results indicate that the positive storm effects are driven by the combined effects of electric field, neutral winds, and composition changes. In this section, we will investigate the relative importance of these processes in producing ionospheric storm effects during the initial phase.

[32] Ionospheric F region ion density changes can be described by the ion continuity equation [Rishbeth and Garriott, 1969, p. 88]:

$$\frac{\partial N}{\partial t} = q - \beta N - \nabla \cdot (N \vec{V}) \quad (1)$$

where N stands for the ion concentration, β is the loss coefficient, and the terms q and βN represent the rate of

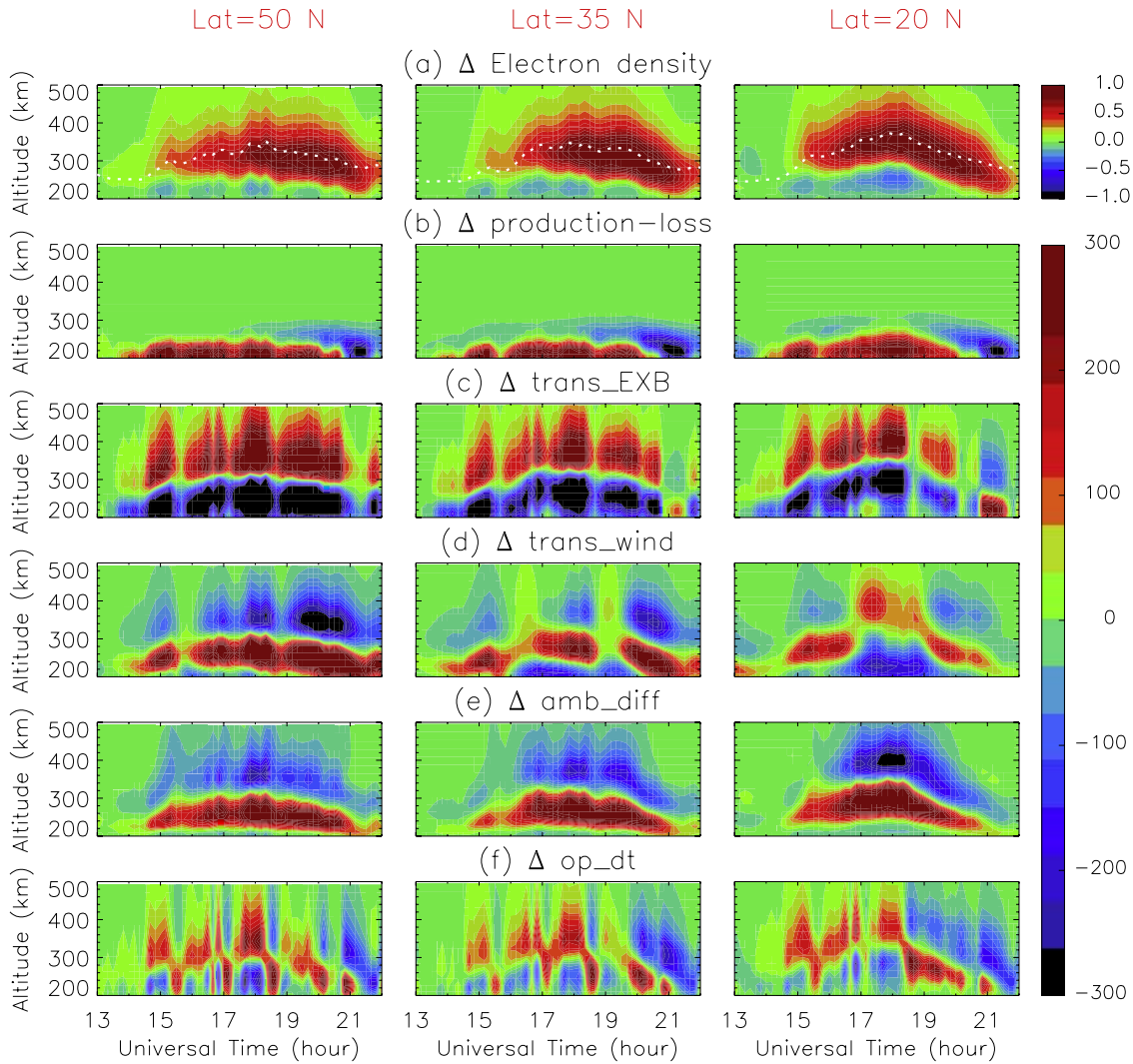


Figure 8. The differences (Storm-Quiet) between the storm-time and quiet (a) electron density (in units of 10^{12} m^{-3}) and (b-f) terms (in units of $10^6 \text{ m}^{-3} \text{ s}^{-1}$) in formula (3). The shown terms are (b) *production - loss*, (c) *trans_E × B*, (d) *trans_{wind}*, (e) *amb_{diff}*, and (f) *op_{dt}*, respectively. The dotted lines in the top panels stand for the corresponding $h_m F_2$ on 14 December. The results are shown for three latitudes in the Northern Hemisphere along the longitude 75°W (LT = UT-5). See the text for more details.

production and loss, respectively. The last term in the right hand side represents transport effects including the transport caused by electric fields, neutral winds, and ambipolar diffusion.

[33] Because the ion composition near the F_2 peak is dominated by O^+ , we will only carry out a term-by-term analysis for the continuity equation of O^+ . Equation (1) can then be rewritten as

$$\frac{\partial N_{\text{O}^+}}{\partial t} = q_{\text{O}^+} - \beta_{\text{O}^+} N_{\text{O}^+} - \nabla \cdot (N_{\text{O}^+} \vec{V}_{\text{O}^+}) \quad (2)$$

[34] For convenience in the following discussion, we denote terms $\frac{\partial N_{\text{O}^+}}{\partial t}$, q_{O^+} and $\beta_{\text{O}^+} N_{\text{O}^+}$ as *op_{dt}*, *production* and *loss*. On the other hand, the transport term $-\nabla \cdot (N_{\text{O}^+} \vec{V}_{\text{O}^+})$ is divided into three parts: transport by electric fields, neutral winds, and ambipolar diffusion. They are denoted as

trans_E × B, *trans_{wind}* and *amb_{diff}*, respectively. From equation (2), we thus have

$$\text{op}_{dt} = \text{production} - \text{loss} + \text{trans}_{E \times B} + \text{trans}_{wind} + \text{amb}_{diff} \quad (3)$$

[35] We will only discuss the effects of vertical drifts and meridional neutral winds on *trans_E × B* and *trans_{wind}*, respectively, because they are the dominant contributions. However, it should be pointed out that *trans_E × B* and *trans_{wind}* from the model also include contributions from zonal drifts and zonal neutral winds, respectively.

5.3.1. North American Sector

[36] Figure 8 shows contours of the differences between the storm- and quiet time electron densities and terms in equation (3) at 75°W for three latitudes (50°N , 35°N , 20°N). The terms are *production-loss*, *trans_E × B*, *trans_{wind}*,

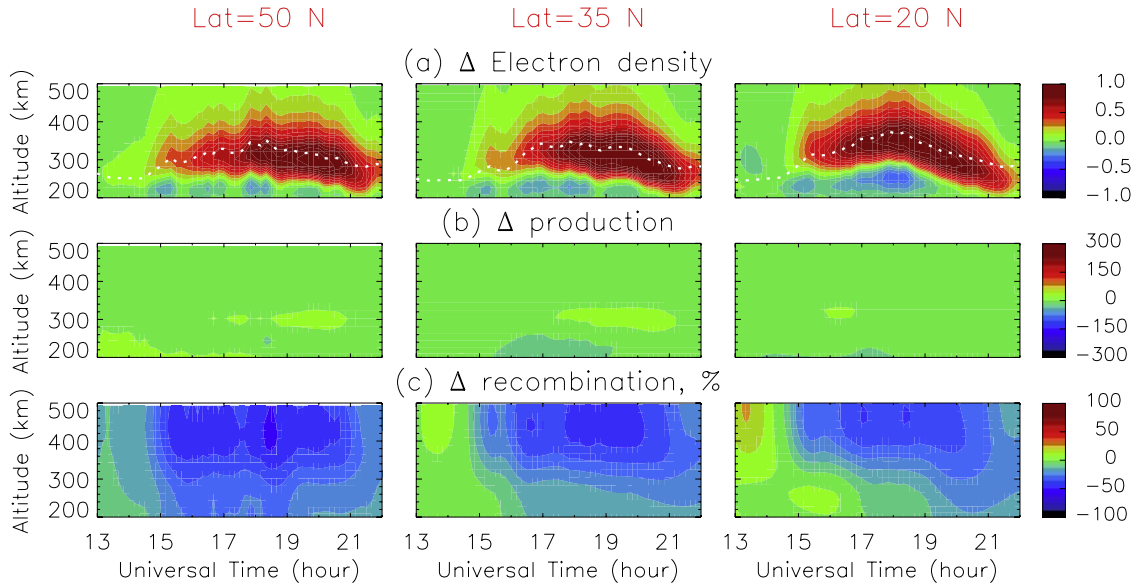


Figure 9. The differences (Storm-Quiet) between the storm-time and quiet (a) electron density (in units of 10^{12} m^{-3}) and (b) *production* (in units of $10^6 \text{ m}^{-3} \text{ s}^{-1}$), and (c) relative changes of loss coefficient β in percent at three northern hemisphere latitudes along the longitude 75°W (LT = UT-5). The dotted lines in the top panels stand for the corresponding h_mF_2 on 14 December. See the text for more details.

amb_diff and *op_dt*, respectively. The increase in electron densities mainly occurs above 250 km at these three latitudes; a decrease in electron densities is weak but visible around 230 km. The changes of the photochemical term, *production-loss* (Figure 8b), are very small above 250 km, and show an increase below 230 km. We will discuss this later. As shown in Figures 6–7, the upward drifts are enhanced in the sunlit sector during this initial phase. The increased upward drifts transport plasma from the bottom side of the *F* region to the topside ionosphere. Thus the term *trans_E × B* increases (positive) in the top side of the *F*₂ layer and decreases (negative) in the bottom side, compared to the quiet time values.

[37] The transport effects of neutral winds are complicated and vary with latitude (Figure 8d). Enhanced northward winds move more ions from the topside to the bottomside ionosphere, whereas southward winds do the opposite. As shown in Figure 6, northward meridional winds become stronger compared with the quiet thermosphere in the higher middle latitudes, whereas they are weaker in the low middle latitudes from 1400 to 1900 UT on 14 December. This can explain why the term *trans_wind* generally decreases in the top side and increases in the bottom side, compared with the quiet values. However, there is an increase of *trans_wind* above about 270 km and a decrease below that height at 35°N and 20°N when the northward meridional winds become weaker during this initial phase.

[38] The term *amb_diff* in Figure 8e is related to the gravity, the gradient of ion concentration and plasma temperature. Because electron densities increase significantly above 250 km (Figure 8a), downward ambipolar diffusion becomes stronger. Therefore the term *amb_diff* decreases in the topside ionosphere and increases in the bottomside ionosphere during this initial phase. Overall, the changes of the terms of *production-loss*, *trans_wind* and *amb_diff* tend to balance those of *trans_E × B*.

[39] The term *op_dt*, the rate of change of O^+ , stands for the net result of the terms in Figures 8b–8e (terms on the right hand side of equation (3)). The net increase of *op_dt* can be seen clearly above 250 km at all latitudes, although the duration of its increase varies with latitude. Obviously, the net increase of *op_dt* above 250 km, which leads to the increase of electron densities, is mainly caused by the increase of *trans_E × B* (Figure 8c), but also has small contributions from neutral wind transport effects at low and middle latitudes (Figure 8d). The increase of *op_dt* oscillates with a period of 1–2 h because the penetration electric fields vary regularly during this initial phase (Figure 7) in association with variations of B_z (Figure 1). The term-by-term analysis reveals that the changes of electric fields play the primary role in the generation of the positive ionospheric storm in North America during the initial phase, while neutral winds also have a role (much smaller) in producing these positive effects.

[40] Figure 9 shows the differences between the storm- and quiet time electron density and *production*, and the relative change of the loss coefficient, $\frac{\beta_{\text{storm}} - \beta_{\text{quiet}}}{\beta_{\text{quiet}}} \times 100\%$ at 75°W for the three latitudes. It can be seen that the change of *production* (Figure 9b) is very small, albeit electron densities increase significantly above 250 km (Figure 9a). This suggests that the changes in the loss term βN should be small. In fact, this is what occurs, because the increase in N (Figure 9a) tends to compensate a decrease in β (Figure 9c) in the topside ionosphere at all three latitudes during the initial phase. The decrease in β is due to an increase of the O/N_2 ratio. Therefore the contribution of the neutral composition changes to the positive storm effects is to decrease β and to offset the effect of increasing electron density, produced by transport processes, on the ion loss term. As a result, the ion loss rate due to chemical processes is almost unchanged for the initial phase of the storm. Crowley *et al.* [2006] reported a similar increase in the electron densities at

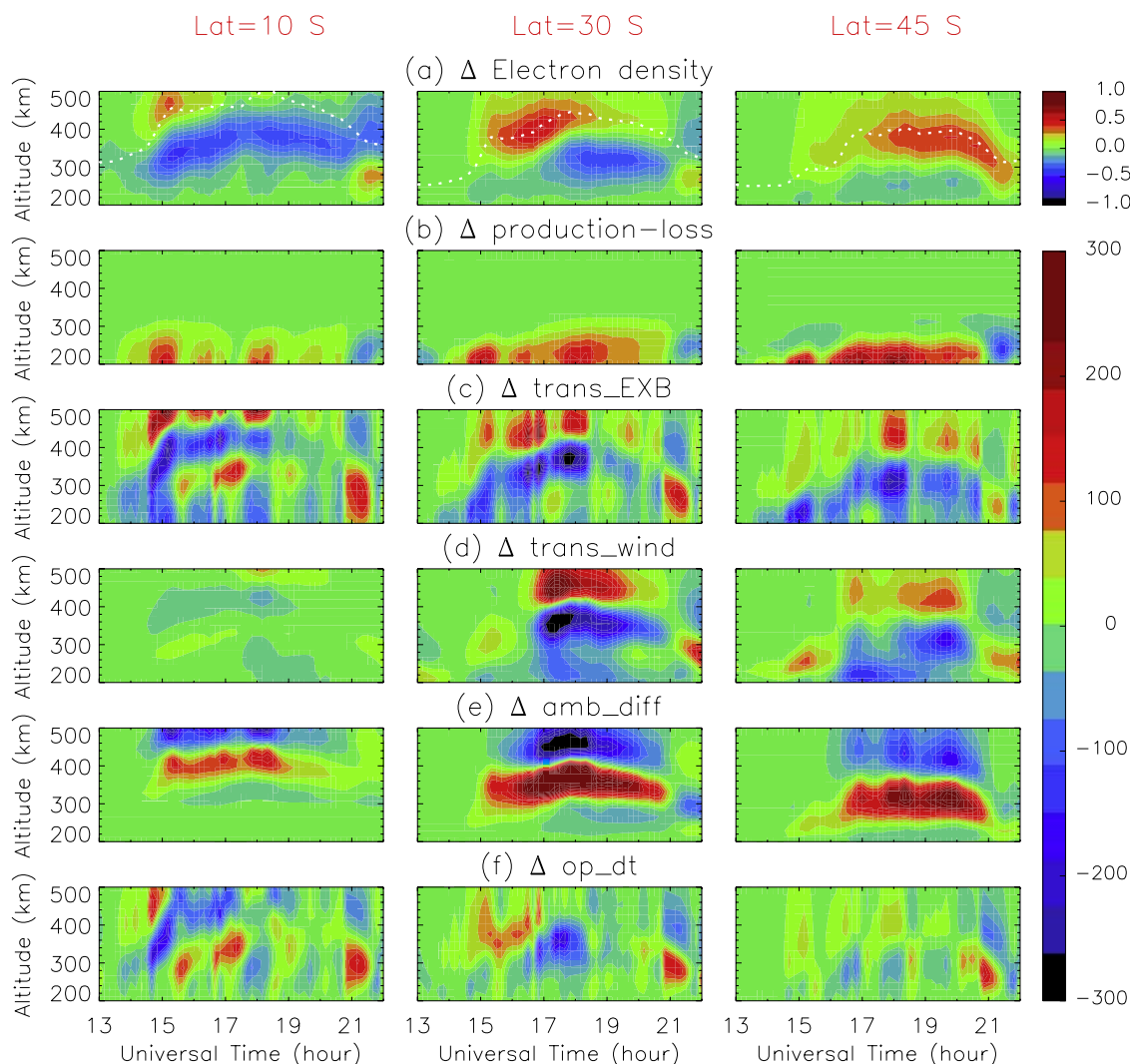


Figure 10. Same as Figure 8, but for the southern hemisphere locations along the longitude 75°W .

the onset of the 20 November 2003 magnetic storm, which was explained by the transport effect of the neutral winds and an increase of O/N_2 .

5.3.2. South American Sector

[41] Figure 10 shows the same fields as Figure 8 but for three southern hemisphere locations (10°S , 30°S and 45°S) along the longitude 75°W . As shown in Figure 10, *production-loss* at these southern hemisphere locations is similar to that at the northern hemisphere locations, that is, the photochemical process does not contribute to the *F* region electron density variations around the *F* region peak during the initial phase of the storm. However, the changes of the electron densities and other terms are significantly different in the two hemispheres. The changes of electron densities in Figure 10a mainly occur above 300 km, and so do the transport terms ($\text{trans}_E \times B$, trans_wind and amb_diff). This is due primarily to the fact that h_mF_2 values are higher in the Southern Hemisphere than in the Northern Hemisphere (Figure 6b).

[42] At 10°S , the changes in the term trans_wind are small. This location is near the magnetic equator so the neutral winds act horizontally and the balance between $\text{trans}_E \times B$ and amb_diff determines the changes of

electron densities given that production-loss changes are small above 300 km. There is an increase of $\text{trans}_E \times B$ above about 440 km and a decrease between about 340 and 440 km, which is caused by the enhanced vertical drifts during this initial phase. The term amb_diff decreases above 440 km and increases below that altitude (in the bottomside ionosphere). Note that the magnetic field line is horizontal at the magnetic equator, so the changes in amb_diff at 10°S come from diffusion horizontally along the field line. The decrease of amb_diff in the topside ionosphere is stronger than (or comparable to) the increase due to $\text{trans}_E \times B$ except during 1400–1500 UT, whereas the increase of amb_diff in the bottom side can not compensate for the decrease due to $\text{trans}_E \times B$, particularly during 1430–1600 UT. Hence there are net decreases of electron density at all altitudes at the magnetic equator except during 1400–1500 UT. The increase of h_mF_2 is mainly caused by the depletion of the bottomside ionosphere, which is of greater magnitude than the decreases of the topside ionosphere.

[43] At 30°S , the changes in the trans_wind term are much greater than those at 10°S . As shown in Figure 6e, meridional winds become much more strongly northward (about 100–200 m/s) in the southern equatorial anomaly

from 1600 to 2000 UT on 14 December. Consequently, at 30°S (which is close to the southern equatorial anomaly), the term $trans_wind$ decreases (is negative) significantly in the bottomside ionosphere and increases (is positive) in the top side during this period because of these strong northward winds. On the other hand, amb_diff decreases above 400 km and increases between 300 and 400 km. However, the increase of amb_diff at about 360 km during 1700–1830 UT is less than the decrease by the transport by $E \times B$ and winds. Thus there is a depletion of the bottomside ionosphere after 1700 UT. *Lei et al.* [2007] showed that, when neutral winds have a strong component along the magnetic field lines that is in the opposite direction to field-aligned diffusion, they may limit the development of the equatorial anomaly. The term analysis supports the suggestion of *Lei et al.* [2007]. Note the increase of topside electron densities before 1900 UT is associated with the increase of $trans_E \times B$.

[44] At 45°S, the temporal variations of the terms are similar to those at 20°N (Figure 8) because these two locations are at approximately conjugate magnetic latitudes. Consequently, the temporal variations of their electron densities are also similar. However, the increase of electron densities at 45°S is much smaller than at 20°N. This is due to the smaller increase of $trans_E \times B$, and thus smaller op_dt in the topside ionosphere at 45°S than at 20°N. This relatively small increase of $trans_E \times B$ in the top side also can be seen in other southern hemisphere locations (for instance at 30°S). As discussed in section 4, the modeled daytime positive storm effects in the South American sector are weaker than in the North American sector, implying that $E \times B$ transport is less effective in the Southern Hemisphere than in the Northern Hemisphere.

5.3.3. Hemispheric Asymmetry of the Positive Storm Effects in the American Sector

[45] Now we attempt to address why these transport effects are weaker in the Southern Hemisphere than in the Northern Hemisphere during this initial phase even though electric fields are very similar in the two hemispheres (Figures 7–8).

[46] The $tran_E \times B$ can be written as $-\nabla \cdot (N_{O^+} \vec{V}_{O^+}^e) \approx -V_{O^+}^e \frac{\partial N_{O^+}}{\partial z}$ in the F_2 region of the middle and high latitudes, where $V_{O^+}^e$ is the vertical component of $E \times B$ drifts and z is altitude. For the same upward drift, the change of $tran_E \times B$ in the top side is thus larger when $-\frac{\partial N_{O^+}}{\partial z}$ is larger, that is, when the O^+ densities in the top side fall off more quickly with altitude. For a given N_{O^+} , $-\frac{\partial N_{O^+}}{\partial z}$ in the topside ionosphere can be considered as the inverse of the effective vertical scale height [*Lei et al.*, 2005; *Liu et al.*, 2007].

[47] Figure 11 shows a set of global maps of H_m near $h_m F_2$ and $-\frac{\partial N_{O^+}}{\partial z}$ at an altitude of $H_m/2$ above $h_m F_2$ from 1600 to 2200 UT on 13 December. H_m is determined from a least squares fitting of the modeled electron density profiles in the lower topside ionosphere using a Chapman function, as described in *Lei et al.* [2005, 2007], but with a scale height independent of altitude. H_m represents the shape of topside profile and depends on plasma temperatures, neutral winds and ambipolar diffusion [*Lei et al.*, 2005; *Liu et al.*, 2007]. Obviously, H_m should be different from the plasma scale height because of the diffusion processes.

[48] As can be seen from Figure 11, $-\frac{\partial N_{O^+}}{\partial z}$ during daytime is smaller at middle and high latitudes in the Southern Hemisphere than in the Northern Hemisphere

because of the larger scale height (left panels of Figure 11) in the summer hemisphere. This change in scale heights is caused by the higher plasma temperatures in the summer hemisphere and the neutral circulation from the summer to the winter hemisphere. Therefore the underestimation of the predicted positive storm in the South American sector indicates that in this event, the model probably overestimates the plasma temperatures in the Southern (summer) Hemisphere or exaggerates the prevailing neutral winds flowing from the summer to the winter hemisphere.

5.3.4. Nighttime Sector

[49] There are no large changes in electron densities in the nighttime sector in the initial phase of this storm, even though $h_m F_2$ increases significantly, as shown in Figure 3. This can also be accounted for by the shape of topside electron density profile. As shown in Figure 11, the effective scale height H_m in the night sector is usually larger than (or comparable to) that at similar latitudes in the daytime sector, whereas the background electron densities at night are much lower. Therefore $-\frac{\partial N_{O^+}}{\partial z}$ ($\approx \frac{N_{O^+}}{H_m}$) in the lower topside ionosphere is small. Note that the effective scale height in the lower topside ionosphere at night is large because of the effects of ambipolar diffusion, although the nighttime plasma scale height is small [*Liu et al.*, 2007].

[50] Small $-\frac{\partial N_{O^+}}{\partial z}$ means that transport via electric field or neutral winds is not able to modify electron densities significantly at night. However, this transport process does deplete the bottomside ionosphere and moves the topside ionosphere upwards, leading to a significant increase of $h_m F_2$ at night.

6. Concluding Remarks

[51] The Coupled Magnetosphere Ionosphere Thermosphere (CMIT) 2.0 model, which couples the NCAR-TIEGCM model with the LFM model, was used to study the response of the thermosphere and ionosphere to the initial phase of the December 2006 geomagnetic storm. The global ionospheric maps of TEC, ionosonde observations at four stations and Millstone Hill ISR measurements were compared with the corresponding simulation results from the CMIT model. Furthermore, a term-by-term analysis for the O^+ continuity equation has been carried out to understand the relative importance of neutral composition, neutral winds and electric fields to the generation of ionospheric storm effects. The main results of this study are as follows:

[52] 1. The global GPS TEC observations showed that pronounced positive storm effects occurred in the American sector during this initial phase, which was driven by the shock associated with the CME. $N_m F_2$ and $h_m F_2$ from the ionosonde and ISR measurements over North America also increased significantly with respect to the quiet time ionosphere after the onset of the storm.

[53] 2. Good agreement between the ionospheric observations and the CMIT simulation was obtained. The CMIT model captured the temporal and spatial variations of the ionospheric storm effects that were seen in the GPS TEC observations. It also reproduced the ionospheric storm effects seen by the ionosondes and the Millstone Hill ISR. There were some quantitative differences, as the model underestimates the magnitude of the increase of the daytime positive effects in the South American sector.

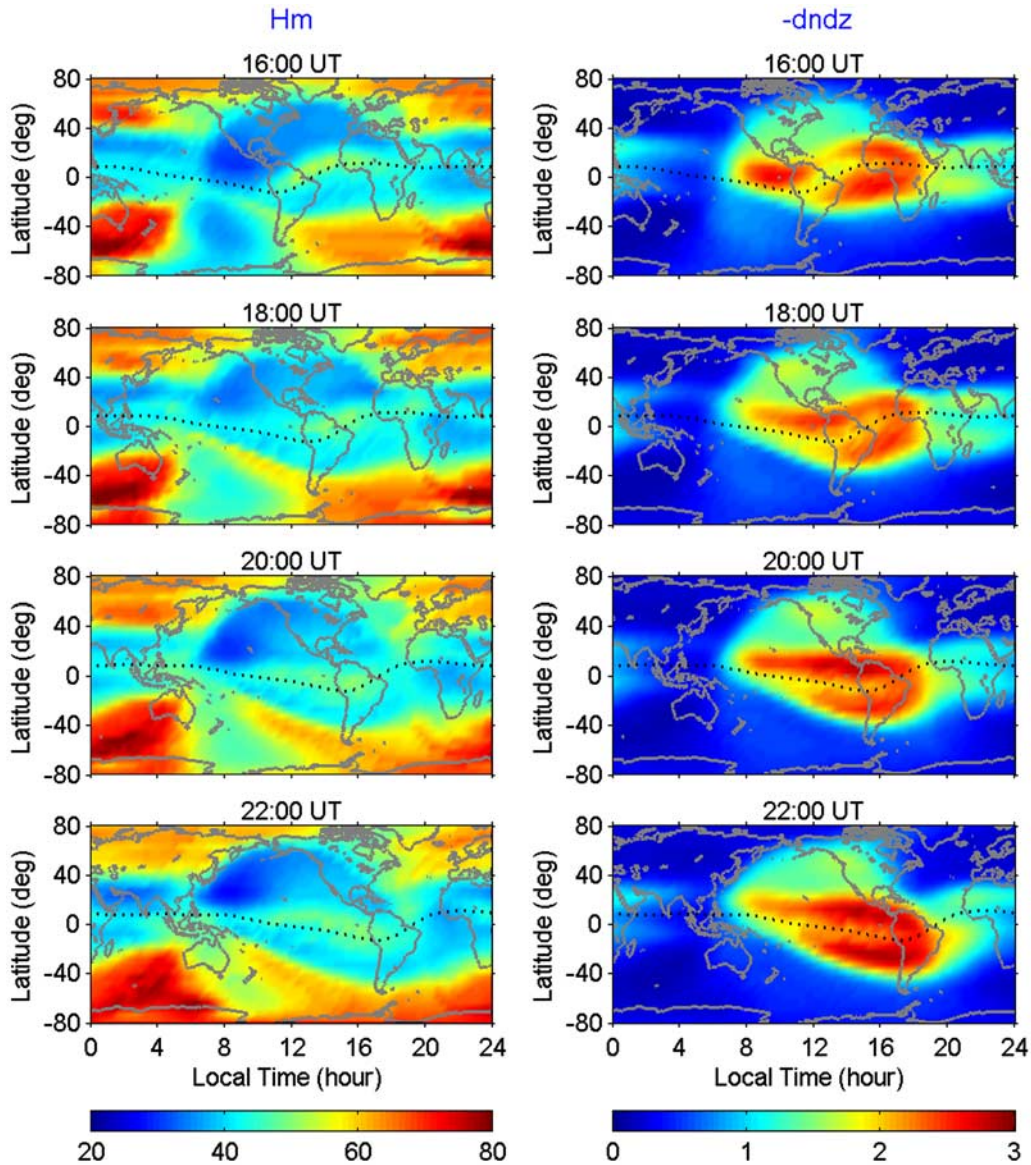


Figure 11. Global maps of the simulated effective scale height H_m (left panels, in units of km) near $h_m F_2$ and $-\frac{\partial N_{O^+}}{\partial z}$ (right panels, in units of 10^6 m^{-4}) at an altitude $H_m/2$ above $h_m F_2$ from 1600 to 2200 UT on 13 December. The dotted lines indicate the location of the magnetic equator.

[54] 3. Our results show that the changes of electric fields are of primary importance in producing the observed positive ionospheric storm in the initial phase of this particular event, whereas neutral winds and composition play a secondary role.

[55] 4. An increase in O/N_2 ratio does not necessarily result in an increase of electron densities in the F_2 region. The decrease in loss coefficient β due to the increase of the O/N_2 ratio is offset by the increasing electron densities, produced by transport processes. Consequently, the ion loss rate due to chemical processes is almost unchanged (Figures 8–10).

[56] 5. Daytime electron densities change less over South America than they do over North America. This is the result of large plasma scale heights near the F_2 peak in the Southern Hemisphere, and the consequent inability of upward motions caused by the given electric fields and

neutral winds to significantly change either $N_m F_2$ or the TEC values. However, the height of the F_2 peak over South America does change significantly as a result of this upward motion.

[57] 6. The model underestimates positive storm effects over the South America. This suggests that the model overestimates plasma temperatures in the Southern (summer) Hemisphere and consequently overestimates the plasma scale height, or exaggerates the prevailing neutral winds which flow from the summer to the winter hemisphere in this event.

[58] 7. The simulations indicated that, at night, the enhanced equatorward disturbed thermospheric winds play a dominant role in producing the increase of $h_m F_2$. However, the variations of electric fields also make contributions to this change in $h_m F_2$. Electron densities at night do not

change significantly, which is the result of the flat electron density profiles above the F_2 peak.

[59] **Acknowledgments.** The Millstone Hill incoherent scatter radar is supported by a cooperative agreement between the National Science Foundation and the Massachusetts Institute of Technology. The ionogram data were obtained from University of Massachusetts Lowell DIDBase, and were also provided by the United States Air Force. The WIND solar wind data were provided by Space Physics Center of UCLA. AE and D_{st} data were obtained from World Data Center in Kyoto; Ap data were from NGDC database. This research was partly supported by the Center for Integrated Space Weather Modeling (CISM) to the National Center for Atmospheric Research (NCAR). NCAR is supported by the National Science Foundation.

[60] Wolfgang Baumjohann thanks Ivan Kutiev and Prof. A. Danilov for their assistance in evaluating this paper.

References

- Bauske, R., and G. W. Pröls (1998), Numerical simulation of long-duration positive ionospheric storm effects, *Adv. Space Res.*, **22**, 117–121.
- Buonsanto, M. J. (1999), Ionospheric storms—A review, *Space Sci. Rev.*, **88**, 563–601.
- Buonsanto, M. J., and O. G. Witasse (1999), An updated climatology of thermospheric neutral winds and F region ion drifts above Millstone Hill, *J. Geophys. Res.*, **104**, 24,675–24,687.
- Burns, A. G., S. C. Solomon, W. Wang, and T. L. Killeen (2007), The ionospheric and thermospheric response to CMEs: Challenges and successes, *J. Atmos. Sol. Terr. Phys.*, **69**, 77–85.
- Crowley, G., et al. (2006), Global thermosphere-ionosphere response to onset of 20 November 2003 magnetic storm, *J. Geophys. Res.*, **111**, A10S18, doi:10.1029/2005JA011518.
- Danilov, A. D., and J. Lastovička (2001), Effects of geomagnetic storms on the ionosphere and atmosphere, *Int. J. Geomagnetism Aeronomy*, **2**, 209–224.
- Fedder, J. A., S. P. Slinker, J. G. Lyon, and R. D. Elphinstone (1995), Global numerical simulation of the growth phase and the expansion onset for a substorm observed by Viking, *J. Geophys. Res.*, **100**, 19,083–19,093.
- Foster, J. C., and A. J. Coster (2007), Conjugate localized enhancement of total electron content at low latitudes in the American sector, *J. Atmos. Sol. Terr. Phys.*, **69**, 1241–1252.
- Fuller-Rowell, T. J., M. V. Codrescu, R. J. Moffett, and S. Quegan (1994), Response of the thermosphere and ionosphere to geomagnetic storms, *J. Geophys. Res.*, **99**, 3893–3914.
- Gonzalez, W. D., J. A. Joselyn, Y. Kamide, H. W. Kroehl, G. Rostoker, B. T. Tsurutani, and V. M. Vasyliunas (1994), What is a geomagnetic storm?, *J. Geophys. Res.*, **99**, 5771–5792.
- Jee, G., A. G. Burns, W. Wang, S. C. Solomon, R. W. Schunk, L. Scherliess, D. C. Thompson, J. J. Sojka, and L. Zhu (2007), Duration of an ionospheric data assimilation initialization of a coupled thermosphere-ionosphere model, *Space Weather*, **5**, S01004, doi:10.1029/2006SW000250.
- Lei, J., L. Liu, W. Wan, and S.-R. Zhang (2005), Variations of electron density based on long-term incoherent scatter radar and ionosonde measurements over Millstone Hill, *Radio Sci.*, **40**, RS2008, doi:10.1029/2004RS003106.
- Lei, J., et al. (2007), Comparison of COSMIC ionospheric measurements with ground-based observations and model predictions: Preliminary results, *J. Geophys. Res.*, **112**, A07308, doi:10.1029/2006JA012240.
- Liu, L., H. Le, W. Wan, M. P. Sulzer, J. Lei, and M.-L. Zhang (2007), An analysis of the scale heights in the lower topside ionosphere based on the Arecibo incoherent scatter radar measurements, *J. Geophys. Res.*, **112**, A06307, doi:10.1029/2007JA012250.
- Lu, G., A. D. Richmond, B. A. Emery, and R. G. Roble (1995), Magnetosphere-ionosphere-thermosphere coupling: Effect of neutral winds on energy transfer and field-aligned current, *J. Geophys. Res.*, **100**(A10), 19,643–19,659.
- Lyon, J. G., J. A. Fedder, and C. M. Mobarry (2004), The Lyon-Fedder-Mobarry (LFM) global MHD magnetospheric simulation code, *J. Atmos. Sol. Terr. Phys.*, **66**, 1333–1350.
- Maruyama, N., A. D. Richmond, T. J. Fuller-Rowell, M. V. Codrescu, S. Sazykin, F. R. Toffoletto, R. W. Spiro, and G. H. Millward (2005), Interaction between direct penetration and disturbance dynamo electric fields in the storm-time equatorial ionosphere, *Geophys. Res. Lett.*, **32**, L17105, doi:10.1029/2005GL023763.
- Mendillo, M. (2006), Storms in the ionosphere: Patterns and processes for total electron content, *Rev. Geophys.*, **44**, RG4001, doi:10.1029/2005RG000193.
- Pröls, G. W. (1993a), On explaining the local time variation of ionospheric storm effects, *Ann. Geophys.*, **11**, 1–9.
- Pröls, G. W. (1993b), Common origin of positive ionospheric storms at middle latitudes and the geomagnetic activity effect at low latitudes, *J. Geophys. Res.*, **98**, 5981–5991.
- Pröls, G. W. (1995), Ionospheric F-region storms, in *Handbook of Atmospheric Electrodynamics*, edited by H. Volland, CRC Press, Boca Raton, Fla.
- Richmond, A. D., E. C. Ridley, and R. G. Roble (1992), A thermosphere/ionosphere general circulation model with coupled electrodynamics, *Geophys. Res. Lett.*, **19**, 601–604.
- Richmond, A. D., C. Peymirat, and R. G. Roble (2003), Long-lasting disturbances in the equatorial ionospheric electric field simulated with a coupled magnetosphere-ionosphere-thermosphere model, *J. Geophys. Res.*, **108**(A3), 1118, doi:10.1029/2002JA009758.
- Rideout, W., and A. Coster (2006), Automated GPS processing for global total electron content data, *GPS Solutions*, doi:10.1007/s10291-006-0029-5.
- Reinisch, B. W., X. Huang, I. A. Galkin, V. Paznukhov, and A. Kozlov (2005), Recent advances in real-time analysis of ionograms and ionospheric drift measurements with digisondes, *J. Atmos. Sol. Terr. Phys.*, **67**, 1054–1062.
- Rishbeth, H., and O. K. Garriott (1969), *Introduction to Ionospheric Physics*, Academic Press, New York.
- Roble, R. G., E. C. Ridley, A. D. Richmond, and R. E. Dickinson (1988), A coupled thermosphere/ionosphere general circulation model, *Geophys. Res. Lett.*, **15**, 1325–1328.
- Szuszczewicz, E. P., M. Lester, P. Wilkinson, P. Blanchard, M. A. Abdu, R. Hanbaba, K. Igarashi, S. Pulinets, and B. M. Reddy (1998), A comparative study of global ionospheric response to intense magnetic storm conditions, *J. Geophys. Res.*, **103**, 11,665–11,684.
- Tsurutani, B., et al. (2004), Global dayside ionospheric uplift and enhancement associated with interplanetary electric fields, *J. Geophys. Res.*, **109**, A08302, doi:10.1029/2003JA010342.
- Wang, W., M. Wiltberger, A. G. Burns, S. C. Solomon, T. L. Killeen, N. Maruyama, and J. Lyon (2004), Initial results from the CISM coupled magnetosphere-ionosphere-thermosphere (CMIT) model: Thermosphere ionosphere responses, *J. Atmos. Sol. Terr. Phys.*, **66**, 1425–1441.
- Wang, W., A. G. Burns, M. Wiltberger, S. C. Solomon, and T. L. Killeen (2006), An analysis of neutral wind generated currents during geomagnetic storms, *J. Atmos. Sol. Terr. Phys.*, **69**, 159–165.
- Wiltberger, M., W. Wang, A. Burns, S. C. Solomon, J. G. Lyon, and C. C. Goodrich (2004), Initial results from the coupled magnetosphere ionosphere thermosphere model: magnetospheric and ionospheric responses, *J. Atmos. Sol. Terr. Phys.*, **66**, 1411–1423.

A. G. Burns, J. Lei, A. D. Richmond, S. C. Solomon, W. Wang, and M. Wiltberger, High Altitude Observatory, National Center for Atmospheric Research, 3080 Center Green, Boulder, CO 80301, USA. (aburns@ucar.edu; leijh@ucar.edu; richmond@ucar.edu; stans@ucar.edu; wbwang@ucar.edu; wiltbemj@ucar.edu)

A. Coster and L. P. Goncharenko, Haystack Observatory, Massachusetts Institute of Technology, Route 40, Westford, Massachusetts, MA 01886, USA.

B. W. Reinisch, Center for Atmospheric Research, University of Massachusetts, Lowell, 600 Suffolk Street, Lowell, MA 01854-3629, USA.